# Comparing the Electronic Structure of Iron, Cobalt, and Nickel Compounds that Feature a Phosphine-Substituted Bis(imino)pyridine Chelate

Matthew R. Mena,<sup>†, ||</sup> Jun-Hyeong Kim,<sup>‡,§, ||</sup> Sangho So,<sup>‡,§</sup> Hagit Ben-Daat,<sup>†</sup> Tyler M. Porter,<sup>†</sup> Chandrani Ghosh,<sup>†</sup> Anuja Sharma,<sup>†</sup> Marco Flores,<sup>†</sup> Thomas L. Groy,<sup>†</sup> Mu-Hyun Baik,\*,<sup>§,‡</sup> Ryan J. Trovitch\*,<sup>†</sup>

<sup>†</sup>School of Molecular Sciences, Arizona State University, Tempe, Arizona 85287, United States <sup>‡</sup>Department of Chemistry, Korea Advanced Institute of Science and Technology (KAIST), Daejeon 34141, Republic of Korea

§Center for Catalytic Hydrocarbon Functionalizations, Institute for Basic Science (IBS), Daejeon 34141, Republic of Korea

# **ABSTRACT**

It was recently discovered that (Ph2PPrPDI)Mn exists as a superposition of low-spin Mn(II) that is supported by a PDI dianion and intermediate-spin Mn(II) that is antiferromagnetically coupled to a triplet PDI dianion, a finding that encouraged the synthesis and electronic structure evaluation of late first row metal variants that feature the same chelate. The addition of Ph2PPrPDI to FeBr2 resulted in bromide dissociation and the formation of [(Ph2PPrPDI)FeBr][Br]. Reduction of this precursor using excess sodium amalgam afforded (Ph2PPrPDI)Fe, which possesses an Fe(II) center that is supported by a dianionic PDI ligand. Similarly, reduction of a pre-mixed solution of Ph2PPrPDI and CoCl2 yielded the cobalt analog, (Ph2PPrPDI)Co. EPR spectroscopy and density functional theory calculations revealed that this compound features a high-spin Co(I) center that is antiferromagnetically coupled to a PDI radical anion. The addition of Ph2PPrPDI to Ni(COD)2 resulted in ligand displacement and the formation of (Ph2PPrPDI)Ni, which was found to possess a pendent phosphine group. Single-crystal X-ray diffraction, CASSCF calculations, and EPR spectroscopy indicate that (Ph2PPrPDI)Ni is best described as having a Ni(II)-PDI<sup>2-</sup> configuration. The electronic differences between these compounds are highlighted and a computational analysis of Ph2PPrPDI denticity has revealed the thermodynamic penalties associated with phosphine dissociation from 5-coordinate (Ph2PPrPDI)Mn, (Ph2PPrPDI)Fe, and (Ph2PPrPDI)Co.

# **INTRODUCTION**

In 2014, we reported that adding the phosphine-substituted bis(imino)pyridine (or pyridine diimine, PDI) chelate Ph2PPrPDI<sup>1</sup> to (THF)<sub>2</sub>MnCl<sub>2</sub> and heating to 90 °C generated the corresponding dichloride compound, (Ph2PPrPDI)MnCl<sub>2</sub>.<sup>2</sup> Reduction of this precursor in the presence of excess sodium amalgam afforded (Ph2PPrPDI)Mn (Figure 1, 1). While formally zerovalent, the solid-state structure of 1 was found to possess PDI bond metrics consistent with two electron ligand reduction.<sup>3,4</sup> At that time, 1 was

proposed to feature a low-spin Mn(II) center and a singlet PDI dianion, an electronic description that is consistent with its ambient temperature magnetic susceptibility (2.2  $\mu_B$ ) and anisotropic EPR spectrum at 77 K ( $S_{Mn} = \frac{1}{2}$ , I = 5/2).<sup>2</sup>

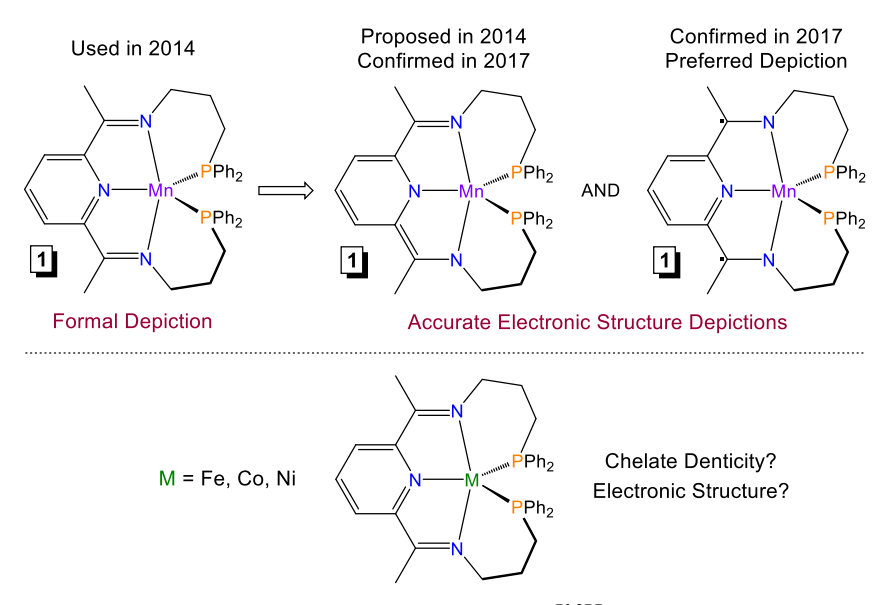


**Figure 1**. Previously described Mn hydrosilylation catalyst (Ph2PPrPDI)Mn (1) and the late first row metal targets that inspired this study.

In a subsequent report, density functional theory (DFT) calculations confirmed that the proposed low-spin doublet configuration was consistent with the experimentally determined solid-state structure. However, non-classical features including a Mulliken spin density of ~1.5 on Mn and irregular Kohn-Sham orbital shapes indicated that this compound could alternatively be described as having an intermediate spin Mn(II) center that is antiferromagnetically coupled to a diradical PDI ligand. This interchangeable and widely-accepted electronic depiction (top right of Figure 1), has been used by our group 4-8 and others 4-14 when highlighting the catalytic activity of 1. Notably, this compound has been reported to catalyze aldehyde hydrosilylation with turnover frequencies (TOFs) of up to 4,900 min<sup>-1</sup>, ketone hydrosilylation with TOFs of up to 1,280 min<sup>-1</sup>, and formate dihydrosilylation with TOFs of up to 330 min<sup>-1</sup>. Due to its activity, 1 has been commercialized by MilliporeSigma, where it is marketed under its formal depiction.

Knowing that **1** exhibits exceptional catalytic activity, an obvious question arises: Can the polydentate redox active ligand <sup>Ph2PPr</sup>PDI be used to prepare 5-coordinate complexes of Fe, Co, or Ni (Figure 1, bottom)? In this study, a unique opportunity to synthesize and compare the electronic structure of compounds that increase in electron count across the late first transition series is described. Preparation of the Fe, Co, and Ni variants is discussed in this contribution, along with coordination and electronic structure differences that were not anticipated at the outset.

# RESULTS AND DISCUSSION

**Synthesis and Electronic Structure Evaluation of** (Ph2PPrPDI)Fe. While modifying the procedure used to synthesize 1,<sup>2</sup> we set out to prepare its formal 18-electron Fe analog. The addition of Ph2PPrPDI<sup>1</sup> to FeBr<sub>2</sub> in THF solution afforded an insoluble purple product upon stirring for 24 h at ambient temperature. Multinuclear NMR spectroscopy revealed that this compound possesses a rotational axis of symmetry, with a single <sup>1</sup>H NMR resonance for the backbone methyl groups located at 1.31 ppm (Figure S3) and a single <sup>31</sup>P NMR environment at 29.64 ppm (Figure S5). The symmetry of this compound, coupled with its lack of solubility and diamagnetism are consistent with pentadentate ligand chelation and formation of the bromide salt, [(Ph2PPrPDI)FeBr][Br] (2, Scheme 1). Taken together, the NMR spectroscopic data suggest that this low-spin Fe(II) compound features a pseudo-octahedral geometry in which the phosphine donor arms are in a *trans*-configuration. It is possible that 2 exists as a 5-coordinate (Ph2PPrPDI)Fe dication with two non-coordinating bromide anions; however, a pseudo trigonal bipyramidal Fe(II)-d<sup>6</sup> complex of this type would be expected to exhibit paramagnetism.

Scheme 1. Preparation of 2 and 3.

Reduction of **2** with excess Na/Hg yielded a greenish-brown product identified as ( $^{Ph2PPr}PDI$ )Fe (**3**, Scheme 1). As observed for compound **2**, the  $^{31}P$  NMR spectrum of **3** features a single resonance at 69.87 ppm, indicating that both chelate phosphine substituents are bound to the iron center. The  $^{1}H$  and  $^{13}C$  NMR spectra similarly suggest that **3** features  $C_2$ -symmetry, given that a single resonance is observed for both backbone methyl groups. In an attempt to uncover additional electronic information, a single crystal of **3** was analyzed by X-ray diffraction and the solid-state structure was found to feature two unique molecules in the asymmetric unit that feature a pentadentate  $^{Ph2PPr}PDI$  chelate (Figure 2 and Figure S1). Each molecule has a pseudo trigonal bipyramidal geometry around iron, with N(1)–Fe(1)–N(3) angles of 159.22(13) and 160.28(11)° and P(1)–Fe(1)–P(2) angles of 102.23(4) and 103.95(3)° for molecules 'A' and 'B', respectively (Table 1). These angles are similar to the same angles determined for Mn complex **1** [157.54(9) and 105.93(3)°]. Notably, the Fe(1)–N(2) lengths found for **3** [1.837(3) and 1.833(2) Å] are considerably shorter than Mn(1)–N(2) length of 1.887(2) Å elucidated for **1**.

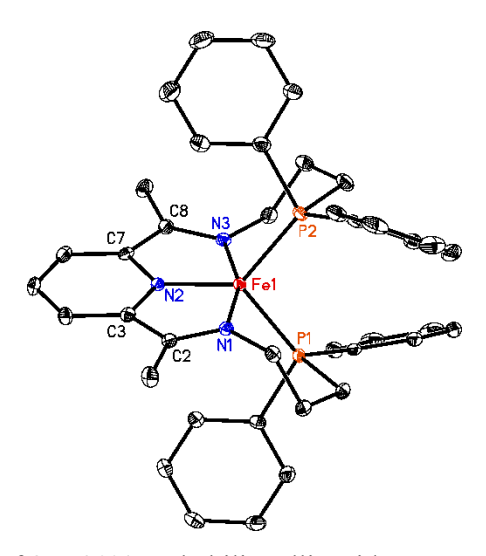


**Figure 2**. Solid-state structure of **3** at 30% probability ellipsoids. Two molecules of **3** were located in the asymmetric unit, molecule 'B' is rendered here. Hydrogen atoms are omitted for clarity.

**Table 1.** Experimentally determined bond lengths (in Å) and angles (in degrees) for 1, 3, and 5, along with calculated values for 3, 4, and 5. For  $3_{exp}$ , values are provided for both molecules in the asymmetric unit.

	<b>1</b> <sup>2</sup> (Mn)	3 <sub>exp</sub> (Fe)	3 <sub>calc</sub> (Fe)	4 <sub>calc</sub> (Co)	5 <sub>exp</sub> (Ni)	<sup>3</sup> 5 <sub>calc</sub> (Ni)	OS5calc (Ni)
M(1)–N(1)	1.944(2)	1.935(3)/1.930(3)	1.951	2.184	1.937(5)	2.110	1.944
M(1)-N(2)	1.887(2)	1.837(3)/1.833(2)	1.827	1.977	1.872(4)	1.941	1.874
M(1)-N(3)	1.949(2)	1.924(3)/1.935(3)	1.953	2.182	1.947(5)	2.118	1.952
M(1)-P(1)	2.2697(8)	2.1795(10)/2.1843(9)	2.166	2.233	2.1574(17)	2.220	2.184
M(1)-P(2)	2.2634(8)	2.1735(10)/2.1768(9)	2.168	2.235	_	_	_
N(1)-C(2)	1.354(3)	1.337(5)/1.338(4)	1.333	1.307	1.340(7)	1.306	1.335
N(3)-C(8)	1.355(3)	1.339(4)/1.341(4)	1.333	1.307	1.337(7)	1.320	1.328
C(2)-C(3)	1.416(4)	1.416(6)/1.422(4)	1.424	1.455	1.427(8)	1.462	1.426
C(7)-C(8)	1.414(3)	1.410(5)/1.418(4)	1.423	1.455	1.429(9)	1.447	1.432
N(1)–M(1)–N(3)	157.54(9)	159.22(13)/160.28(11	160.4	152.3	150.8(2)	156.2	154.4
P(1)-M(1)-P(2)	105.93(3)	102.23(4)/103.95(3)	103.9	100.6	_ ` `	_	_
N(2)-M(1)-P(1)	130.90(6)	130.95(9)/128.01(8)	128.4	129.8	151.01(15)	169.3	148.5
N(2)-M(1)-P(2)	123.14(6)	126.81(9)/128.04(8)	127.7	129.6	- ` ´	-	-

Bis(imino)pyridine ligands are known to behave in a redox non-innocent fashion when coordinated to low-valent first row metals, <sup>15-18</sup> and intraligand bond lengths can provide insight into how many electrons have been transferred from the metal into the chelate  $\pi$ -system. <sup>19,20</sup> The average imine C=N bond length determined for **3** is 1.34 Å and the average backbone C-C bond length is 1.42 Å, metrics that suggest a singly or doubly reduced PDI ligand according to bond lengths tabulated by Budzelaar. <sup>3</sup> Wieghardt and coworkers recently described a new parameter,  $\Delta_{exp}$ , which subtracts the average imine and pyridine C-N length from the average backbone C-C length. <sup>21</sup> The  $\Delta_{exp}$  value for **3** is 0.054 Å, which is consistent with 2-electron PDI reduction.

To gain additional insight into the electronic structure of **3**, DFT calculations were performed and the frontier molecular orbital diagram of this complex is shown in Figure 3. The HOMO, labeled as PDI-1π\*, features π-bonding between d<sub>xz</sub> and the b<sub>2</sub> orbital of PDI. This interaction leads to a relatively short Fe(1)–N(2) bond length, determined to be 1.837(3) and 1.833(2) Å by single crystal X-ray diffraction. At 42%, PDI-based orbitals contribute nearly twice as much to the composition of the HOMO than Fe-based orbitals, which contribute only 23%. The next highest occupied orbitals HOMO–1, HOMO–2, and HOMO–3 are dominated by contributions from the iron-based d<sub>z²</sub>, d<sub>yz</sub>, and d<sub>xy</sub> orbitals, as illustrated in Figure 3. Therefore, the electronic structure is most consistent with an Fe(II)-d<sup>6</sup> center that is supported by a singlet PDI dianion, as indicated for **3** in Scheme 1.<sup>22</sup>

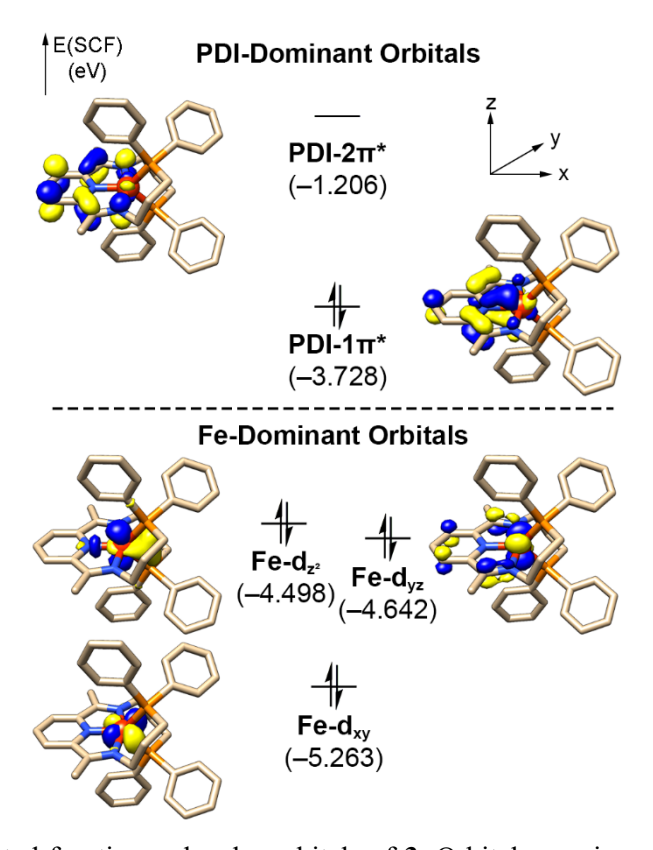


**Figure 3.** DFT-calculated frontier molecular orbitals of **3**. Orbital energies are given in eV. Contour isovalue of 0.05 is used. Hydrogen atoms are omitted for clarity.

Synthesis and Electronic Structure Evaluation of ( $^{Ph2PPr}PDI$ )Co. Synthesis of the cobalt analog commenced with the addition of  $^{Ph2PPr}PDI$  to  $CoCl_2$  in THF solution. After stirring for 2 h at ambient temperature, reduction with excess Na/Hg in the presence of catalytic 1,3,5,7-cyclooctatetraene<sup>2</sup> afforded a red product identified as ( $^{Ph2PPr}PDI$ )Co (4, Scheme 2). In contrast to the data collected for 2 and 3, compound 4 was found to exhibit paramagnetically broadened  $^{1}H$  NMR resonances over a 100-ppm shift range at ambient temperature (Figure S9). Moreover, 4 was found to exhibit an effective magnetic moment of 1.67  $\mu_B$  at 25  $^{\circ}C$ , which is consistent with the presence of a single unpaired electron.

# Scheme 2. Synthesis of 4.

To obtain additional electronic information, the X-band (9.40 GHz) electron paramagnetic resonance (EPR) spectrum of 4 was recorded in a toluene glass at 115 K (Figure 4). The observed spectral features are consistent with the presence of a  $S = \frac{1}{2}$  species, with a signal centered around the magnetic field value corresponding to g = 2.0 (Figure 4). In addition, the spectrum was found to feature a multiline pattern due to hyperfine coupling (hfc) between the magnetic moment of the unpaired electron and the magnetic moment of a  $^{59}$ Co (I = 7/2) nucleus.

To obtain the EPR parameters, the respective spin Hamiltonian was fit to the data (Figure 4, dotted line). The EPR spectrum of 4 was well-fit ( $\sigma = 2.8$  %, see Experimental Details) considering one unpaired electron on a <sup>59</sup>Co center ( $S_{\text{Co}} = \frac{1}{2}$ , I = 7/2) with anisotropic g values ( $g_x = 2.120$ ,  $g_y = 2.105$ ,  $g_z = 1.969$ ) and large anisotropic hyperfine couplings ( $|A_x| = 334.0$ ,  $|A_y| = 154.6$ ,  $|A_z| = 1.6$  MHz) (see Table 2). These properties are similar to those previously reported for the <sup>55</sup>Mn center ( $S_{\text{Mn}} = \frac{1}{2}$ , I = 5/2) in compound 1,<sup>2</sup> suggesting that the coordination environment about Co in 4 is similar to the crystallographically determined coordination environment about Mn in 1. In summary, the EPR spectrum of 5 is consistent with the presence of a single unpaired electron on Co ( $S_{\text{Co}} = \frac{1}{2}$ ).

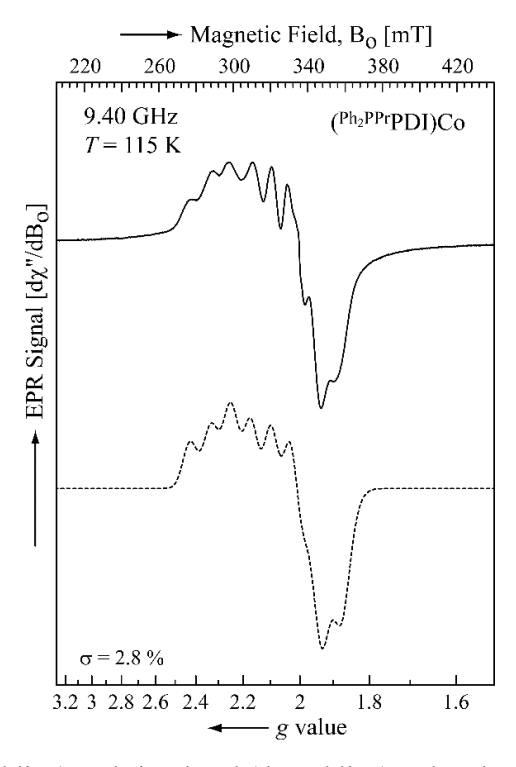


Figure 4. Experimental (solid line) and simulated (dotted line) X-band EPR spectra of 4 at 115 K.

**Table 2.** Parameters used to fit the EPR spectra of 1, 4, and 5 at X-band (9.4 GHz) and low temperature.

Parameter <sup>a</sup>	$(Mn)^2$ (T = 77  K)	<b>4</b> (Co) ( <i>T</i> = 115 K)	$5 (Ni)^b$ ( $T = 112 K$ )
$g_x$	2.079	2.120	2.199
$g_y$	2.037	2.105	2.125
$g_z$	2.017	1.969	2.023
$ A_x $ (MHz)	161.2	334.0	_c
$ A_y $ (MHz)	375.4	154.6	_
$ A_z $ (MHz)	164.8	1.6	_
$\Delta B_x$ (MHz)	152.2	257.9	296.6
$\Delta B_y$ (MHz)	162.7	405.9	279.9
$\Delta B_z$ (MHz)	112.4	520.4	270.8

<sup>&</sup>lt;sup>a</sup> The fitting parameters were the principal components of g (i.e.  $g_x$ ,  $g_y$ , and  $g_z$ ), the principal components of the hfc tensor A (i.e.  $A_x$ ,  $A_y$ , and  $A_z$ ), and the peak-to-peak line widths ( $\Delta B_x$ ,  $\Delta B_y$ , and  $\Delta B_z$ ). <sup>b</sup> The EPR spectrum of this compound showed the signals of two S = 1/2 spins, one corresponding to Ni(I) (for parameters see at the table) and another one corresponding to a ligand radical (PDI<sup>-</sup>) with the following parameters:  $g_x = 2.012$ ,  $g_y = 2.005$ , and  $g_z = 1.991$ ;  $\Delta B_x = 61.8$  MHz,  $\Delta B_y = 59.4$  MHz, and  $\Delta B_z = 105.4$  MHz. <sup>c 61</sup>Ni has nuclear spin (I = 3/2) but its natural abundance is only 1.14%, so the respective hfc interaction cannot be resolved.

Calculations were also carried out to gain additional electronic information. DFT predicts that the ground state of **4** is a doublet. The quartet state, which features a PDI radical anion that is not coupled to two unpaired Co electrons, was determined to be 14.5 kcal/mol higher in energy. The calculated molecular orbitals of **4** are illustrated in Figure 5. Similar to **3**, the PDI- $1\pi^*$  orbital is mainly composed of the PDI  $b_2$  orbital with minimal Co- $d_{xz}$  contribution, and is singly occupied by a down-spin electron. There are a total of eight Co d-electrons; Co- $d_{z^2}$ , Co- $d_{yz}$ , and Co- $d_{xy}$  are occupied with two electrons while Co- $d_{x^2-y^2}$  and Co- $d_{xz}$  feature one electron each. The calculated spin density illustrates two up-spin electrons on the Co and one down-spin electron on the PDI ligand, which implies antiferromagnetic coupling between the high-spin Co(I) center and the PDI radical anion. Taken together, our computational results are consistent with the experimental assignment, in which a PDI radical anion is antiferromagnetically coupled to a high-spin Co(I) center.

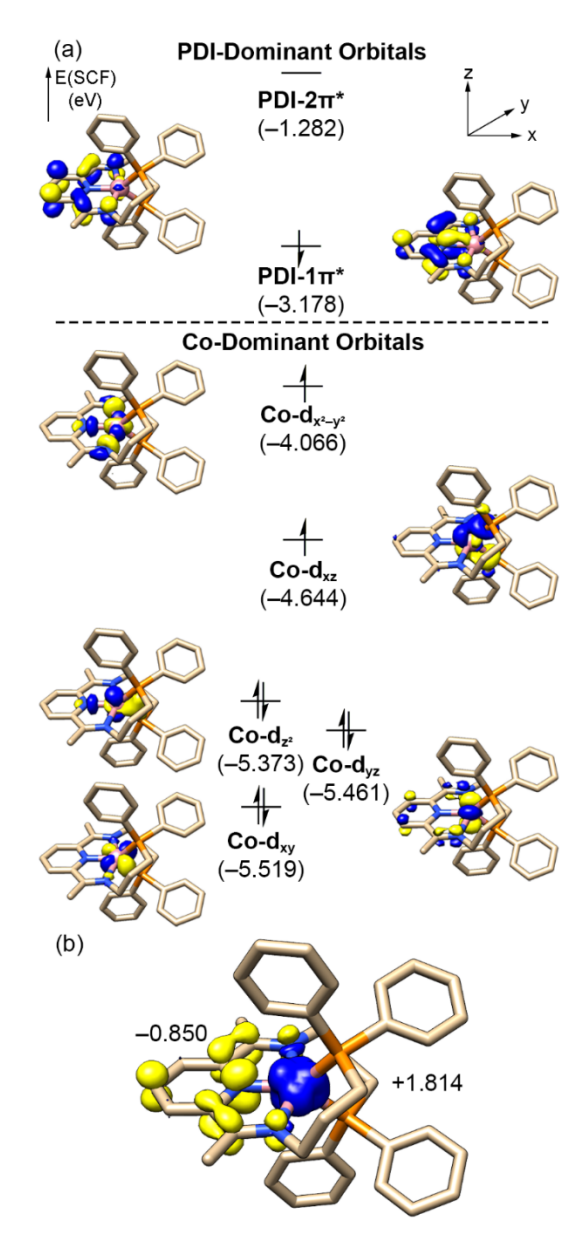


**Figure 5.** DFT-calculated (a) frontier molecular orbitals and (b) Mulliken spin density plot of **4**. Orbital energies are given in eV. Contour isovalue of 0.05 and 0.005 is used for (a) and (b), respectively. Hydrogen atoms are omitted for clarity.

Synthesis and Electronic Structure Evaluation of ( $^{Ph2PPr}PDI$ )Ni. In order to prepare the Ni variant envisioned in Figure 1, the readily available Ni(0) precursor Ni(COD)<sub>2</sub> was added to a toluene solution of  $^{Ph2PPr}PDI$ . After stirring at ambient temperature for 24 h, filtering the reaction, and removing liberated COD and solvent under vacuum, an olive-green product identified as ( $^{Ph2PPr}PDI$ )Ni (5, Scheme 3) was obtained. The  $^{1}H$  NMR spectrum of this complex was found to feature paramagnetically-broadened resonances over a 30-ppm range (Figure S10). This observation was quite surprising since we had targeted a diamagnetic, formal 20-electron complex that was predicted to possess a chelate dianion (Figure 1). Interestingly, 5 was found to exhibit a solution magnetic moment of 1.23  $\mu_B$  at 25 °C, which is lower than the spin-only value expected for a single unpaired electron. The magnetic susceptibility

of crystalline 5 was found to be even lower (0.33  $\mu_B$  at 25 °C, magnetic susceptibility balance), a value that is within the error expected for a diamagnetic complex.<sup>25</sup>

## **Scheme 3.** Preparation of **5**.

To gain additional insight, a single crystal of this complex was analyzed by X-ray diffraction. The solid-state structure of **5** was found to possess a  $\kappa^4$ -N,N,N,P- $^{Ph2PP}$ PDI chelate (Figure 6), where the coordinated phosphine moiety deviates significantly from the PDI plane with a N(2)–Ni(1)–P(1) angle of only 151.01(15)°. Notably, the PDI chelate features elongated N(1)–C(2) and N(3)–C(8) lengths of 1.340(7) and 1.337(7) Å, along with contracted C(2)–C(3) and C(7)–C(8) lengths of 1.427(8) and 1.429(9) Å, respectively. These metrics are consistent with a singly- or doubly-reduced PDI ligand according to bond lengths proposed by Budzelaar. The  $\Delta_{exp}$  value for **5** as defined by Wieghardt is 0.067 Å, which lies within the range that has previously been assigned to 2-electron PDI reduction (0.044–0.069 Å).

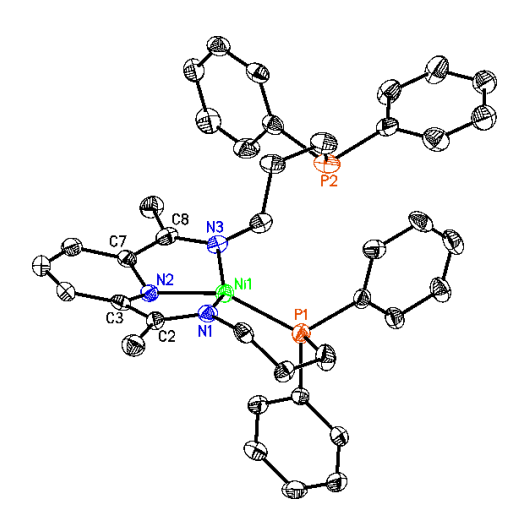
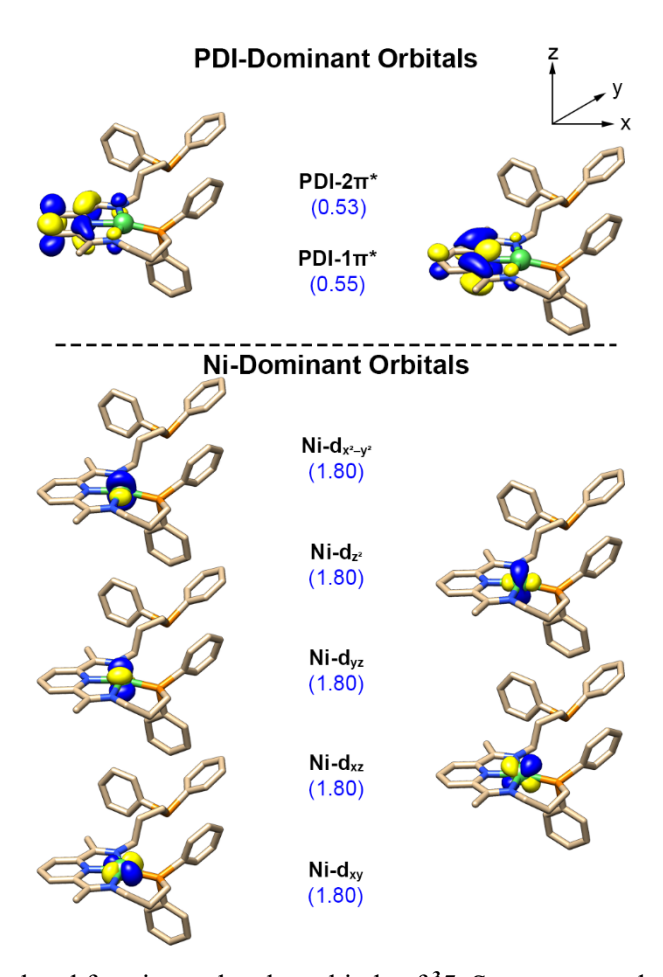


Figure 6. Solid-state structure of 5 at 30% probability ellipsoids. Hydrogen atoms are omitted for clarity.

DFT calculations were then performed for **5** and the frontier molecular orbitals are provided in Figure S12. The  $b_2$  orbital of PDI (PDI- $1\pi^*$ ) was found to be singly occupied while the high-lying PDI- $2\pi^*$  orbital was found to be empty. A total of 9 d-electrons were located in Ni-dominant orbitals. In addition, the two magnetic orbitals (Ni- $d_{x^2-y^2}$  and PDI- $1\pi^*$ ) were found to be spatially orthogonal, indicating that the unpaired electrons cannot exchange. Interestingly, DFT also predicts that the openshell singlet of **5**, which features antiferromagnetically coupled ligand and Ni-based radicals, is only

1.3 kcal/mol higher in energy. The low magnetic susceptibilities observed for 5 at 25 °C suggested the presence of this state. Therefore, state-averaged CASSCF (SA-CASSCF) calculations, whose electronic states are corrected by N-Electron Valence Perturbation Second Order (NEVPT2) theory, were carried out since DFT may not be capable of providing a reliable spin state energy difference. The electronic structure from the CAS calculations is summarized in Figure 7 and the corresponding ground state composition is enumerated in Table 3. The triplet ( ${}^35$ -T<sub>0</sub>) decomposed into two major configurations,  ${}^3\Phi_1$  and  ${}^3\Phi_2$ , amounting to 58 and 37%, respectively. Taking a deeper look at each configuration,  ${}^3\Phi_1$  represents a state consistent with the singly-occupied Ni-d<sub>x²-y²</sub> and PDI-1 $\pi^*$  orbitals that DFT suggests. The  ${}^3\Phi_2$  state is associated with singly-occupied Ni-d<sub>z²</sub> and PDI-1 $\pi^*$  orbitals. Both configurations feature the unpaired electron in PDI-1 $\pi^*$  with nine Ni-d electrons, suggesting Ni(I)–PDI<sup>--</sup> character to  ${}^35$ -T<sub>0</sub>. The putative singlet state ( ${}^35$ -S<sub>1</sub>), whose electronic structure is constructed by flipping the spin of the PDI-based unpaired electron in  ${}^3\Phi_1$  and  ${}^3\Phi_2$ , is only 1.6 kcal/mol higher in energy, which may enable fast intersystem crossing between the two spin states in solution.  ${}^{23,24}$ 



**Figure 7.** CAS(16,10)-calculated frontier molecular orbitals of <sup>3</sup>**5**. State-averaged occupation numbers projected into natural orbital manifolds are highlighted in blue. Contour isovalue of 0.05 is used. Hydrogen atoms are omitted for clarity.

In Wieghardt and coworkers' review of structurally characterized PDI complexes,<sup>21</sup> monohalide<sup>26</sup> and monomethyl compounds<sup>27</sup> of Ni that feature a PDI radical anion were found to exhibit  $\Delta_{exp}$  values

of 0.112 and 0.095 Å, respectively, while diamagnetic ( $^{2,6\text{-iPr}_2\text{Ar}}\text{PDI}$ )Ni(N<sub>2</sub>) was assigned to possess a PDI dianion with a  $\Delta_{\text{exp}}$  value of 0.067 Å.<sup>27</sup> The  $\Delta_{\text{exp}}$  value of 0.067 Å determined for 5 suggests the presence of a PDI dianion, which is not consistent with the calculations described for the triplet-optimized structure ( $^{3}$ 5). In the molecular structure of 5 (Figure 6), the Ni center lies out of the PDI plane with a calculated geometry index ( $\tau_4$ )<sup>28</sup> of 0.412. A  $\tau_4$  value of only 0.245 was determined for  $^{3}$ 5 (Figure 7), which is more consistent with an overall square planar geometry. In contrast, a  $\tau_4$  value of 0.405 was calculated for the open-shell singlet-optimized structure,  $^{08}$ 5. This value is consistent with the crystal structure, implying that 5 adopts an open-shell singlet in the solid-state. Accordingly, the low magnetic susceptibility of crystalline 5 (0.33  $\mu_{\text{B}}$  at 25 °C) is consistent with the presence of  $^{08}$ 5.

To further understand the electronic structure of os5, SA-CASSCF/NEVPT2 calculations were carried out and the results are summarized in Figure 8. The projection allows orbital mixing between PDI-based orbitals (possibly due to orbital localization), producing PDI- $1\pi$ \* and PDI- $2\pi$ \* (which are similar to the LUMO of diimine ligands). Evaluating the degree of PDI reduction by counting the number of electrons in these orbitals remains valid due to the antibonding character on the imines and bonding character on the backbone C-C bond. Our calculations predict that the singlet ground state of the given structure ( $^{\text{OS}}5-\text{S}_0$ ) is 16.0 kcal/mol lower than the putative triplet state ( $^{\text{OS}}5-\text{T}_1$ ) and has two predominant configurations,  ${}^{1}\Phi_{1}$  and  ${}^{1}\Phi_{2}$ , whose weights are 26 and 11%, respectively (See Table 3). Leading contribution  ${}^{1}\Phi_{1}$  shows unpaired electrons in the PDI- $1\pi$ '\* and PDI- $2\pi$ '\* orbitals as well as singly-occupied Ni- $d_{yz}$  and Ni- $d_{x^2-y^2}$  orbitals. State  ${}^1\Phi_2$  features singly-occupied PDI- $1\pi$ '\*, PDI- $2\pi$ '\*,  $Ni-d_{yz}$ , and  $Ni-d_{z^2}$ , as listed in Table 3. Thus, both configurations are best assigned to  $Ni(II)-PDI^{2-}$  and consist of a total 37% of OS5-S<sub>0</sub>, suggesting a Ni(II)-PDI<sup>2-</sup> assignment for the crystal structure of 5. We analyzed the character of all configurations and found that <sup>OS</sup>5-S<sub>0</sub> features a 50% Ni(II)-PDI<sup>2-</sup> contribution, negligible Ni(I)-PDI<sup>-</sup> contribution (2%), and no Ni(0)-PDI<sup>0</sup> or Ni(III)-PDI<sup>3-</sup> contribution. The residual 49% comes from several excited state configurations whose individual weights are less than 7%. For example, the most dominant excited state configuration in OS5-S0 contributes 6% and represents a PDI  $\pi$ - $\pi$ \* transition. While the configurations provide interesting information on 5, deducing a relevant Lewis structure from a spin-adapted configuration is problematic (e.g., where the up and down-spin unpaired electrons are located). To provide additional insight, the two major configurations are decomposed into Slater determinants:

$$\begin{split} ^{1}\Phi_{1} &= +\ 0.1265(|(d_{yz})^{\uparrow}(d_{x^{2}-y^{2}})^{\downarrow}(1\pi^{\prime\ast})^{\uparrow}(2\pi^{\prime\ast})^{\downarrow}| + |(d_{yz})^{\downarrow}(d_{x^{2}-y^{2}})^{\uparrow}(1\pi^{\prime\ast})^{\downarrow}(2\pi^{\prime\ast})^{\uparrow}|) \\ &+ 0.1641(|(d_{yz})^{\uparrow}(d_{x^{2}-y^{2}})^{\downarrow}(1\pi^{\prime\ast})^{\downarrow}(2\pi^{\prime\ast})^{\uparrow}| + |(d_{yz})^{\downarrow}(d_{x^{2}-y^{2}})^{\uparrow}(1\pi^{\prime\ast})^{\uparrow}(2\pi^{\prime\ast})^{\downarrow}|) \\ &- 0.2906(|(d_{yz})^{\uparrow}(d_{x^{2}-y^{2}})^{\uparrow}(1\pi^{\prime\ast})^{\downarrow}(2\pi^{\prime\ast})^{\downarrow}| + |(d_{yz})^{\downarrow}(d_{x^{2}-y^{2}})^{\downarrow}(1\pi^{\prime\ast})^{\uparrow}(2\pi^{\prime\ast})^{\uparrow}|) \\ ^{1}\Phi_{2} &= +\ 0.1124(|(d_{yz})^{\uparrow}(d_{z^{2}})^{\downarrow}(1\pi^{\prime\ast})^{\downarrow}(2\pi^{\prime\ast})^{\uparrow}| + |(d_{yz})^{\downarrow}(d_{z^{2}})^{\uparrow}(1\pi^{\prime\ast})^{\uparrow}(2\pi^{\prime\ast})^{\downarrow}|) \\ &+ 0.0878(|(d_{yz})^{\uparrow}(d_{z^{2}})^{\downarrow}(1\pi^{\prime\ast})^{\uparrow}(2\pi^{\prime\ast})^{\downarrow}| + |(d_{yz})^{\downarrow}(d_{z^{2}})^{\uparrow}(1\pi^{\prime\ast})^{\downarrow}(2\pi^{\prime\ast})^{\uparrow}|) \\ &- 0.1942(|(d_{yz})^{\uparrow}(d_{z^{2}})^{\uparrow}(1\pi^{\prime\ast})^{\downarrow}(2\pi^{\prime\ast})^{\downarrow}| + |(d_{yz})^{\downarrow}(d_{z^{2}})^{\downarrow}(1\pi^{\prime\ast})^{\uparrow}(2\pi^{\prime\ast})^{\uparrow}|) \end{split}$$

In both configurations, determinants whose configuration interaction (CI) coefficient is positive represent two antiparallel unpaired electrons in the Ni- and the PDI-based orbitals and are best described as  $S_{\text{Ni}} = 0$  with  $S_{\text{PDI}} = 0$ . In contrast, determinants with negative CI coefficients show two parallel unpaired electrons in the Ni- and the PDI-based orbitals, indicating antiferromagnetic coupling between  $S_{\text{Ni}} = 1$  and  $S_{\text{PDI}} = 1$ . These results allow us to assign the Lewis structure shown in Scheme 3 and Figure 9a, where triplet/singlet Ni(II) is coordinated by a triplet/singlet PDI dianion. Taken together, our detailed electronic structure analysis suggests that 5 adopts a singlet Ni(II)-PDI<sup>2-</sup> electronic structure in the solid-state, which exists as an ensemble average of  $S_{\text{Ni}} = 0$  with  $S_{\text{PDI}} = 0$  and  $S_{\text{Ni}} = 1$  antiferromagnetically coupled to  $S_{\text{PDI}} = 1$ .

**Table 3.** NEVPT2/SA-CASSCF(16,10)-computed configurations of <sup>3</sup>5-T<sub>0</sub> and <sup>OS</sup>5-S<sub>0</sub>. Configurations of more than 10% weight are given below.

		Weight	Electronic Configuration	Character
<sup>3</sup> 5-T <sub>0</sub>	$^{3}\Phi_{1}$	58.08	$(d_{xy})^2(d_{xz})^2(d_{yz})^2(d_{z^2})^2(d_{x^2-y^2})^1(1\pi^*)^1(2\pi^*)^0$	Ni(I)–PDI*
	$^{3}\Phi_{2}$	36.55	$(d_{xy})^2(d_{xz})^2(d_{yz})^2(d_{z^2})^1(d_{x^2-y^2})^2(1\pi^*)^1(2\pi^*)^0$	Ni(I)-PDI*-
<sup>OS</sup> 5-S <sub>0</sub>	$^{1}\Phi_{1}$	25.48	$(d_{xy})^2(d_{xz})^2(d_{yz})^1(d_{z^2})^2(d_{x^2-y^2})^1(1\pi'^*)^1(2\pi'^*)^1$	Ni(II)-PDI <sup>2-</sup>
	$^{1}\Phi_{2}$	11.40	$(d_{xy})^2(d_{xz})^2(d_{yz})^1(d_{z^2})^1(d_{x^2-y^2})^2(1\pi'^*)^1(2\pi'^*)^1$	Ni(II)-PDI <sup>2-</sup>

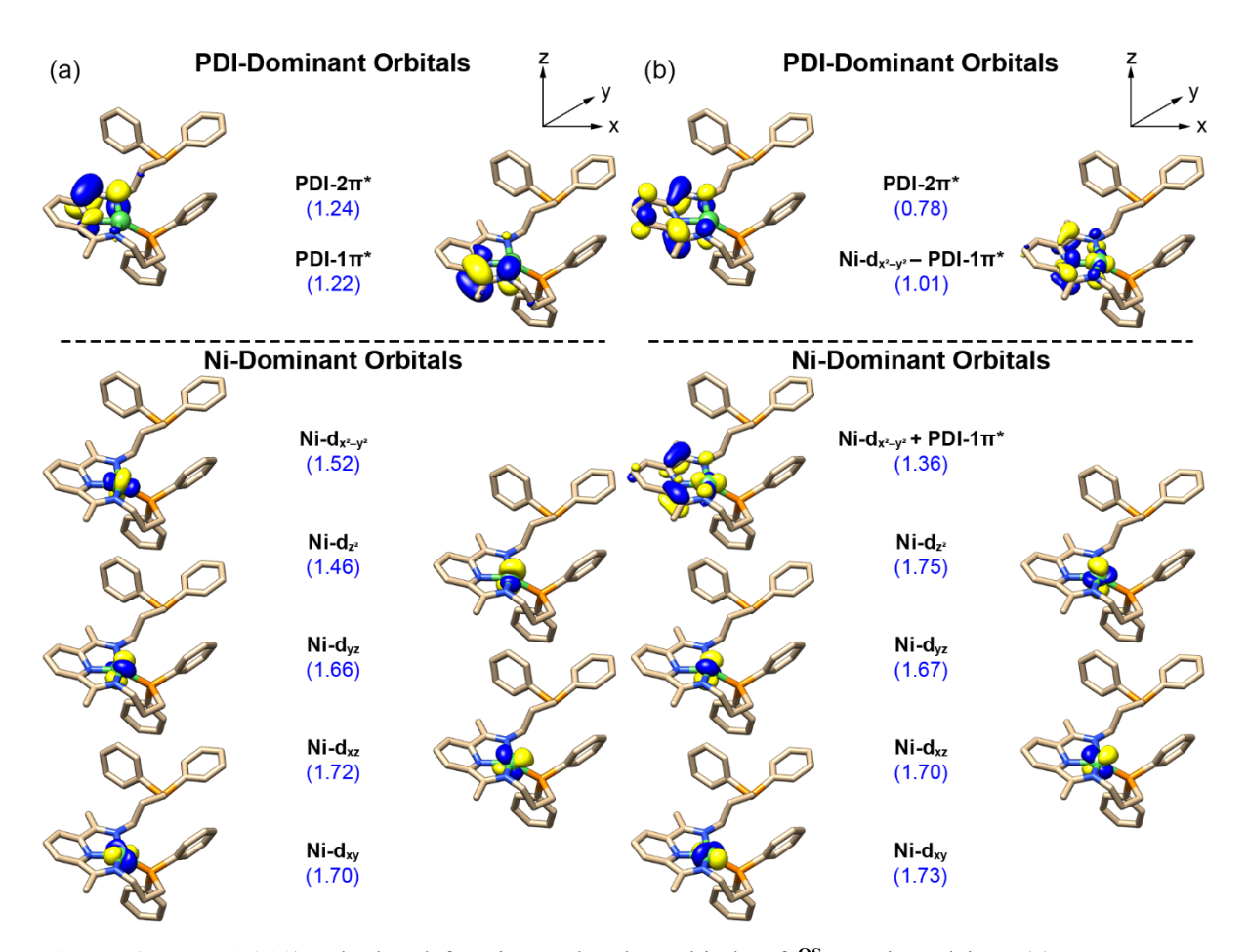


**Figure 8.** CAS(16,10)-calculated frontier molecular orbitals of <sup>os</sup>**5** projected into (a) Forster-Boys localized orbitals and (b) natural orbitals. A state-averaged occupation number projected into an orbital manifold is highlighted in blue. Contour isovalue of 0.05 is used. Hydrogen atoms are omitted for clarity.

Our calculations also show that  $^35$  features a N(2)–Ni(1)–P(1) angle of 169.3° with a calculated  $\tau_4$  value of 0.245, which is the closest the Ni(I) complex can come to exhibiting idealized square planar geometry. This geometry can be accessed in solution due to thermal motion of the coordinated phosphine substituent and the turning off of metal-to-ligand antiferromagnetic coupling. The optimized structure of  $^35$  is interesting because Ni(I) complexes generally adopt a distorted tetrahedral structure and have an occupied Ni- $^{1}d_{x^2-y^2}$  orbital which repels the ligands around the Ni center, pulling it out of the ligand plane. We carefully compared the electronic differences between  $^{3}5$  and  $^{08}5$ , whose geometry is calculated to be tetrahedral for the same reason. A notable difference can be found when the CAS-wavefunction of  $^{08}5$  is projected into natural orbitals. As illustrated in Figure 9b, the nickel ion deviating from the PDI plane allows interaction between the Ni- $^{1}d_{x^2-y^2}$  and the PDI- $^{1}\pi^*$  orbital, an interaction that could not be identified for  $^{3}5$ . In other words, unlike  $^{08}5$ ,  $^{3}5$  is unable to mix orbitals and remains square planar. The Ni- $^{1}d_{x^2-y^2}$  and the PDI- $^{1}\pi^*$  orbitals of  $^{3}5$  are occupied by up-spin electrons and mixing yields significant Pauli repulsion, which does not allow orbital interactions between the same spin. Thus,  $^{3}5$  adopts a distorted square planar structure because the driving force that renders the structure tetrahedral (Ni- $^{1}d_{x^2-y^2}$  + PDI- $^{1}\pi^*$ ) is absent.

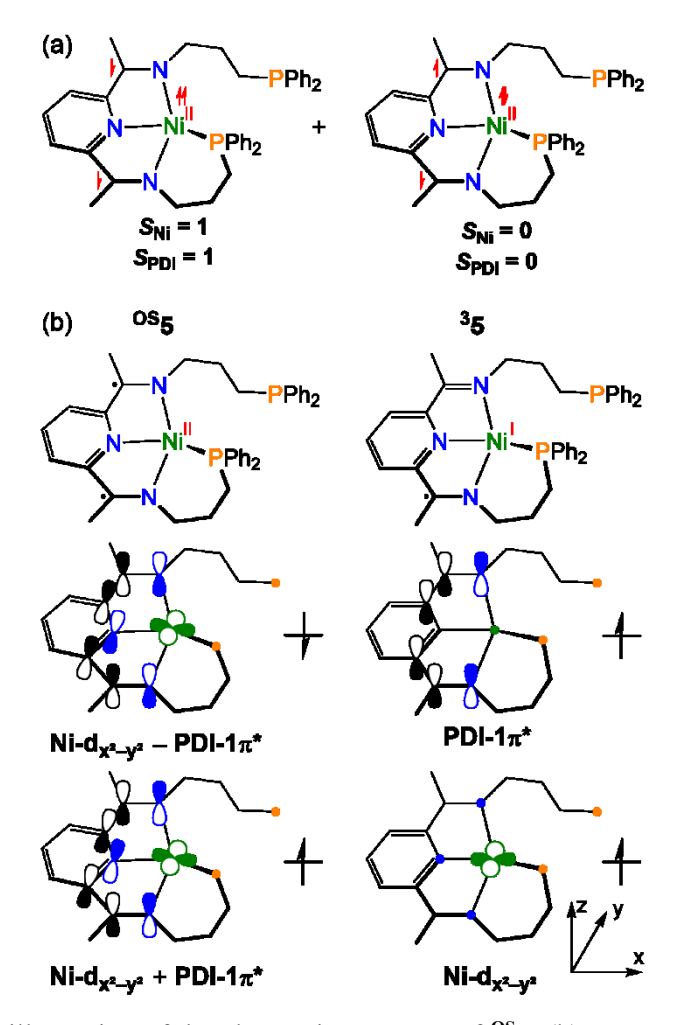


**Figure 9.** (a) Schematic illustration of the electronic structure of <sup>OS</sup>5. (b) Conceptual MO diagram of <sup>OS</sup>5 (left) and <sup>3</sup>5 (right).

To reconcile the fact that  $^{OS}5$  is diamagnetic, yet a modest magnetic susceptibility (1.23  $\mu$ B, 25 °C) was noted in solution, the X-band (9.40 GHz) EPR spectrum of 5 was recorded in a toluene glass at 112 K (Figure 10). The observed spectrum is an overlap of two  $S = \frac{1}{2}$  signals, a slightly broadened isotropic signal located at the magnetic field value corresponding to g = 2.0 and a very broad signal showing significant rhombic g anisotropy. To obtain the EPR parameters, the respective spin Hamiltonian was fit to the data (Figure 10, red line) while assuming that the broad signal belongs to Ni(I) ( $S_{Ni} = \frac{1}{2}$ ) (Figure 10, dashed line) and the narrow signal belongs to an unpaired electron located within a PDI ligand (PDI<sup>-</sup>) (Figure 10, dotted line). The spectral features observed for 5 were well-fit ( $\sigma = 0.6\%$ , see Experimental Details) upon assigning a 95% contribution to Ni(I) and a 5% contribution to the PDI radical anion (Figure S11). This ratio was found to be consistent across three different concentrations of 5 in toluene, suggesting that dilution does not influence the ratio of unpaired electrons present.

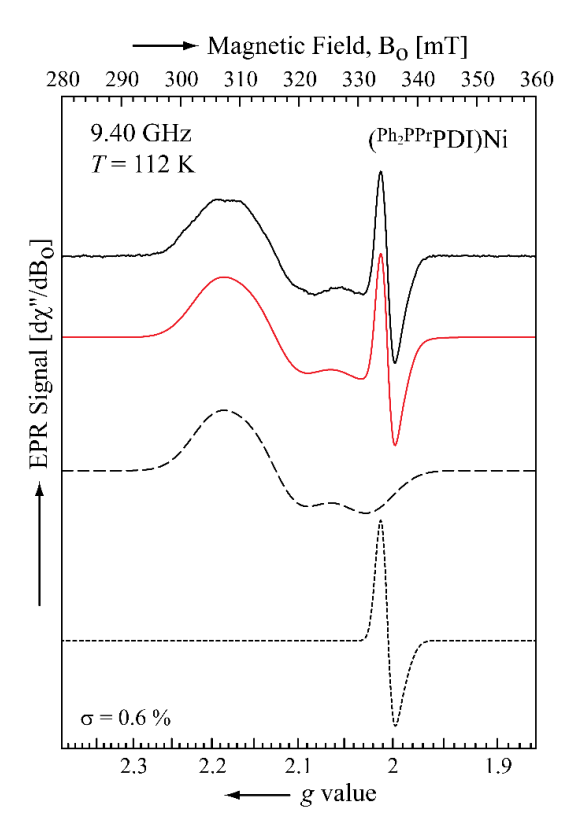


**Figure 10.** Experimental (solid black line) and simulated (solid red line) X-band EPR spectra of **5** at 112 K. Simulation of the spectral components corresponding to a Ni(I) center (dashed line) and a PDI radical anion (dotted line) are also shown. The sum of the spectral components results in the simulated spectrum (solid red line).

A spin-counting experiment was also performed to determine the quantity of spin present in a solution of 5 relative to an equimolar solution of 4 using the same tube and settings. Comparison of the total double integrals revealed that the sample of 5 possessed only 39% of the spin present in the sample of 4. Upon assigning the narrow signal to the ligand-based unpaired electron of  $^35$ , the unpaired electron associated with the Ni(I) center of  $^35$  can be estimated to account for 5% of the overall signal that is observed. The unpaired electrons of  $^35$  are in orthogonal orbitals that cannot participate in exchange; however, a through-space interaction between these electrons is responsible for broadening of the PDI-based signal to 24 G. Although it remains an open question at this time, the excess  $S_{\text{Ni}} = \frac{1}{2}$  signal may be due to the formation of additional Ni(I) species upon disproportionation of the PDI-based electron. Accounting for this additional spin, and the fact that  $^35$  possesses two spins per molecule, it is estimated that 63% of solution-based 5 is present as EPR silent  $^{\text{OS}}5$ . This is consistent with the low magnetic susceptibility observed for 5 in solution. It also confirms that 5 is most appropriately thought of as a Ni(II) complex that features a PDI dianion.

Thermodynamic Penalties Associated with Phosphine Dissociation. Considering that 5 possesses a tetradentate ligand while 1, 3, and 4 do not, the thermodynamic benefit associated with  $\kappa^5$ - versus  $\kappa^4$ Ph2PPrPDI coordination to Mn, Fe, and Co was also explored. For Mn compound 1, DFT calculations

reveal that  $\kappa^{5\text{-Ph2PPr}}\text{PDI}$  binding provides a thermodynamic benefit of only 2.6 kcal/mol over  $\kappa^{4\text{-}}$   $P,N,N,N^{-\text{Ph2PPr}}\text{PDI}$  coordination (1', Figure 11). In contrast, iron compound 3 was found to be 32.5 kcal/mol more stable than  $(\kappa^{4\text{-}}P,N,N,N^{-\text{Ph2PPr}}\text{PDI})\text{Fe}$  (3'). The ground state of 4 was determined to be 12.4 kcal/mol lower in energy than the putative 4-coordinate analog  $(\kappa^{4\text{-}}P,N,N,N^{-\text{Ph2PPr}}\text{PDI})\text{Co}$  (4'). The energies summarized in Figure 11 can be rationalized by the presence, or absence, of frontier molecular orbitals that feature M–P  $\sigma^*$  character. For example, the  $d_{xz}$  orbital of 4 (Figure 5) possesses considerable M–P  $\sigma^*$  character, leading to a modest M–P bond strength of 12.4 kcal/mol. In comparison, the frontier molecular orbitals of 3 (Figure 3) exhibit no M–P  $\sigma^*$  character, which results in phosphine dissociation being particularly unfavorable.

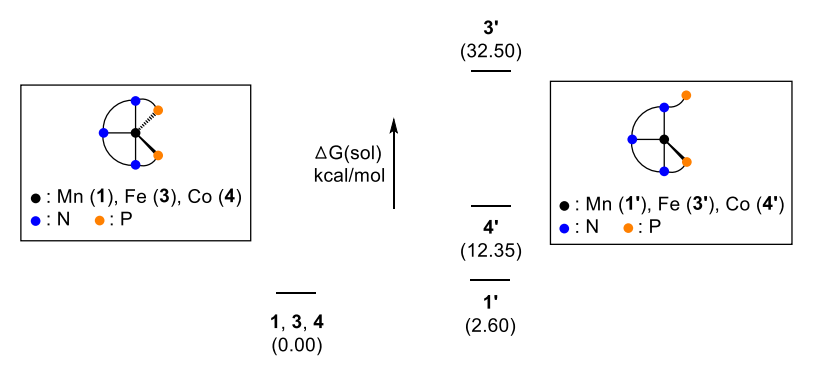


Figure 11. DFT-calculated energies for phosphine-dissociated compounds 1', 3', and 4'.

Electronic Similarities and Differences. Although similarities exist, each (Ph2PPPPDI)M compound discussed in this study has a distinct electronic structure. For example, compounds 1, 3, and 5 all feature a doubly reduced PDI chelate and a divalent metal center. However, compounds 1 and 5 can be drawn as two different resonance forms (Figures 1 and 9a), while the only accurate electronic depiction of 3 features a PDI singlet dianion. Compound 5 is clearly distinct from 1 in that it features a 4-coordinate ligand and has the ability to access a different geometry and spin state due to the thermal motion of its coordinated phosphine substituent. The ground state of 4 and 35 both feature a singly reduced PDI chelate, but the former exhibits Co-PDI antiferromagnetic coupling while the latter has been observed to feature uncoupled Ni and PDI-based electrons in solution. The energetically-preferred states of 1 and 4 feature a metal-based electron that is not engaged in antiferromagnetic coupling to a ligand-based radical, suggesting that these compounds have the potential to act as metalloradicals.

For readers who are unfamiliar with electron counting and determining coordinative saturation for complexes that feature redox non-innocent chelates, a summary of these concepts for each (Ph2PPrDI)M compound is offered. For example, **1** has a *formal electron count* of 17, which assumes that all ligand-stored electrons are available to the Mn center (this transfer of electrons is commonly observed for redox-active ligands). <sup>5,7,14,16-18</sup> In contrast, **1** has an *actual electron count* of 15, indicating that this compound has the ability to coordinate a small and neutral sixth ligand. This characteristic has already been demonstrated given the isolation of (Ph2PPrPDI)Mn(CO). <sup>29</sup> Iron compound **3** is a formal 18 electron

complex and has an actual electron count of 16, indicating that it may also be capable of binding a sixth ligand. Interestingly, 4 has a formal electron count of 19, which is consistent with the presence of a reduced PDI chelate. With an actual electron count of 18, 4 is unlikely to bind an incoming substrate prior to phosphine arm dissociation. Finally, 5 is formally an 18-electron complex and its predominant electronic structure features an electron count of 16.

# **CONCLUSION**

By extending the coordination chemistry of  $^{Ph2PPT}PDI$  to late first row transition metals, a variety of denticities and electronic structures were uncovered. The reduction of  $[(^{Ph2PPT}PDI)FeBT][BT]$  allowed for the isolation of  $(^{Ph2PPT}PDI)Fe$ , which was found to feature a pentadentate ligand, an Fe(II) center, and a singlet PDI dianion. In contrast,  $(^{Ph2PPT}PDI)Co$  was found to possess a high-spin Co(I) center where one of two unpaired electrons is antiferromagnetically coupled to a PDI radical anion. The electronic structure of  $(^{Ph2PPT}PDI)Ni$  was found to be particularly intriguing. Crystalline  $(^{Ph2PPT}PDI)Ni$  was found to be diamagnetic and calculations revealed that its solid-state structure exists as an open-shell singlet having a Ni(II) center and a PDI dianion that is best described as an ensemble average of  $S_{Ni} = 0$  with  $S_{PDI} = 0$  and  $S_{Ni} = 1$  antiferromagnetically coupled to  $S_{PDI} = 1$ . The EPR spectrum of this complex at 112 K also revealed the presence of uncoupled Ni and PDI-based electrons and NEVPT2/CASSCF predicted that the Ni(I) compound featuring a PDI radical anion could be accessed. The relative ease of phosphine dissociation from  $(\kappa^5 - ^{Ph2PPT}PDI)M$  complexes has also been evaluated, revealing the following M–P bond dissociation energy relationship:  $(\kappa^5 - ^{Ph2PPT}PDI)Mn < (\kappa^5 - ^{Ph2PPT}PDI)Co < (\kappa^5 - ^{Ph2PPT}PDI)Fe.$ 

# **EXPERIMENTAL DETAILS**

General Considerations. All reactions were performed inside an MBraun glovebox under an atmosphere of purified nitrogen. Toluene, tetrahydrofuran, pentane, and diethyl ether were purchased from Sigma-Aldrich, purified using a Pure Process Technology solvent system, and stored in the glovebox over activated 4 Å molecular sieves and potassium before use. Benzene-*d*<sub>6</sub>, acetone-*d*<sub>6</sub>, acetonitrile-*d*<sub>3</sub>, and chloroform-*d* were purchased from Oakwood Chemicals and dried over 4 Å molecular sieves (and potassium in the case of benzene-*d*<sub>6</sub>). 2,6-Diacetylpyridine was obtained from Oakwood Chemicals, while cobalt dichloride was obtained from Strem. Ph2PPTPDI was synthesized according to literature procedures. Celite was purchased from Acros. Solution H NMR spectra were recorded at room temperature on a Varian 400-MR (400 MHz), Varian 500-MR (500 MHz), Bruker Ascend 400 MHz, or Bruker Ascend 500 MHz NMR spectrometer. All H NMR and <sup>13</sup>C NMR chemical shifts are reported in parts per million relative to Si(CH<sub>3</sub>)<sub>4</sub> using internal Si(CH<sub>3</sub>)<sub>4</sub> or <sup>1</sup>H (residual) and <sup>13</sup>C chemical shifts of the solvent as secondary standards. <sup>31</sup>P NMR chemical shifts are reported in parts per million relative to H<sub>3</sub>PO<sub>4</sub>. Elemental analyses were performed at Robertson Microlit Laboratories,

Inc. (Ledgewood, NJ). Solution-state magnetic susceptibility was determined via the Evans method on the Varian 400-MR (400 MHz) NMR spectrometer.

X-ray crystallography. Single crystals suitable for X-ray diffraction were coated with polyisobutylene oil in the glovebox and transferred to glass fiber with Apiezon N grease before mounting on the goniometer head of a Bruker APEX Diffractometer (Arizona State University) equipped with Mo Kα radiation. A hemisphere routine was used for data collection and determination of the lattice constants. The space group was identified and the data was processed using the Bruker SAINT+ program and corrected for absorption using SADABS. The structures were solved using direct methods (SHELXS) completed by subsequent Fourier synthesis and refined by full-matrix, least-squares procedures on [F²] (SHELXL). For complex 3, two unique molecules were located in the asymmetric unit. The structure of 5 was found to possess one positionally disordered propylene substituent. For tables of crystallographic and metrical parameters, see the Supporting Information.

# **Electron Paramagnetic Resonance Spectroscopy.**

Instrumentation. Studies were performed at the EPR Laboratory, part of the Chemical and Environmental Characterization Core Facilities at Arizona State University. Continuous wave (CW) EPR spectra were recorded at 115 K for 4 and 112 K for 5 using a Bruker ELEXSYS E580 CW X-band spectrometer (Bruker, Rheinstetten, Germany) equipped with a liquid nitrogen temperature control system (ER 4131VT). The magnetic field modulation frequency was 100 kHz with a field modulation amplitude of 1 mT peak-to-peak. The microwave power was 4 mW for 4 and 1 mW for 5, the microwave frequency was 9.40 GHz and the sweep time was 168 seconds for 4 and 84 seconds for 5.

Spin Hamiltonian. The EPR spectrum of **4** was interpreted using a S =  $\frac{1}{2}$  spin Hamiltonian, H, containing the electron Zeeman interaction with the applied magnetic field **B**<sub>0</sub>, and hyperfine coupling (hfc) interaction with the  $^{59}$ Co (I =  $^{7/2}$ ) nucleus: $^{30}$ 

$$H = \beta_e \mathbf{S} \cdot \mathbf{g} \cdot \mathbf{B_0} + h \mathbf{S} \cdot \mathbf{A} \cdot \mathbf{I}$$
 (1)

where **S** is the electron spin operator, **I** is the nuclear spin operator of  $^{59}$ Co, **A** is the hfc tensor in frequency units, **g** is the electronic g-tensor,  $\beta_e$  is the electron magneton, and h is Planck's constant.

The EPR spectrum of **5** was analyzed considering that the molecule contains two  $S = \frac{1}{2}$  spins. One corresponds to the unpaired electron of a Ni(I) center (denoted by  $S_A$ ) and the other belongs to the unpaired electron at the PDI radical anion (denoted by  $S_B$ ). They interact with the applied magnetic field  $B_0$  (Zeeman interaction) but not with each other. The spin Hamiltonian, H', of this system is:

$$H' = \beta_e S_A . g_{Ni} . B_0 + \beta_e S_B . g_{PDI} . B_0$$
 (2)

where  $S_A$  and  $S_B$  are the corresponding electron spin operators,  $g_{Ni}$  and  $g_{PDI}$  are the electronic g-tensors for the Ni(I) center and the PDI radical anion, respectively.

Fitting of EPR spectra. To quantitatively compare experimental and simulated spectra, we divided the spectra into N intervals (i.e., we treated the spectrum as an N-dimensional vector  $\mathbf{R}$ ). Each component  $R_j$  has the amplitude of the EPR signal at a magnetic field  $B_j$ , with j varying from 1 to N. The amplitudes

of the experimental and simulated spectra were normalized so that the span between the maximum and minimum values of  $R_j$  is 1. We compared the calculated amplitudes  $R_j^{calc}$  of the signal with the observed values  $R_j$  defining a root-mean-square deviation s by:

$$\sigma(p_1,\,p_2,...,\,p_n) = \big[ \sum\limits_{j} \big( R_j^{calc}(p_1,\,p_2,\,...,\,p_n) - R_j^{exp} \big)^2 / N \big]^{1/2} \eqno(3)$$

where the sums are over the N values of j, and p's are the fitting parameters that produced the calculated spectrum. For our simulations, N was set equal to 2048 for 4 and 1024 for 5. The EPR spectra were simulated using EasySpin (v 5.2.25), a computational package developed by Stoll and Schweiger<sup>31</sup> and based on Matlab (The MathWorks, Natick, MA, USA). EasySpin calculates EPR resonance fields using the energies of the states of the spin system obtained by direct diagonalization of the spin Hamiltonian (see Eqs. 1 and 2). The EPR fitting procedure used a Monte Carlo type iteration to minimize the root-mean-square deviation,  $\sigma$  (see Eq. 3) between measured and simulated spectra. We searched for the optimum values of the following parameters: the principal components of g (i.e.  $g_x$ ,  $g_y$ , and  $g_z$ ), the principal components of the hfc tensor A (i.e.  $A_x$ ,  $A_y$ , and  $A_z$ ) and the peak-to-peak linewidths ( $\Delta B_x$ ,  $\Delta B_y$ , and  $\Delta B_z$ ).

# **COMPUTATIONAL DETAILS**

Computational details. All calculations were carried out using DFT<sup>32</sup> as implemented in the Jaguar 9.1 suite<sup>33</sup> of ab initio quantum chemistry programs. Geometry optimizations were performed with M06<sup>34</sup> functional and the 6-31G\*\* basis set<sup>35</sup> for main group atoms. Fe, Co, and Ni were represented using the Los Alamos LACVP basis. 36-38 The energies of the optimized structures were reevaluated by additional single-point calculations on each optimized geometry using B3LYP-D3 functional 39-45 with Dunning's correlation consistent triple-ζ basis set cc-pVTZ(-f), 46 which includes a double set of polarization functions. For Fe, Co, and Ni, we used a modified version of LACVP, designated as LACV3P, in which the exponents were decontracted to match the effective core potential with triple-ζ quality. Solvation energies were evaluated by a self-consistent reaction field (SCRF) approach based on accurate numerical solutions of the Poisson-Boltzmann equation. In the results reported, solvation calculations were carried out with the 6-31G\*\*/LACVP basis at the optimized gas-phase geometry employing the dielectric constants of  $\varepsilon = 7.6$  and 2.379 for THF and toluene, respectively. As is the case for all continuum models, the solvation energies are subject to empirical parametrization of the atomic radii that are used to generate the solute surface. We employed the standard set of optimized radii in Jaguar for H (1.150 Å), C (1.900 Å), N (1.600 Å), P (2.074 Å), Fe (1.456 Å), Co (1.436 Å), and Ni (1.417 Å). Analytical vibrational frequencies within the harmonic approximation were computed with the 6-31G\*\*/LACVP basis to confirm proper convergence to well-defined minima or saddle points on the potential energy surface. The energy components have been computed with the following protocol. The free energy in solution-phase, G(sol), has been calculated as follows:

$$G(\text{sol}) = G(\text{gas}) + G_{\text{solv}}$$
 (4)

$$G(gas) = H(gas) - TS(gas)$$
 (5)

$$H(gas) = E(SCF) + ZPE$$
 (6)

$$\Delta E(SCF) = \sum E(SCF)$$
 for products  $-\sum E(SCF)$  for reactants (7)

$$\Delta G(\text{sol}) = \sum G(\text{sol}) \text{ for products} - \sum G(\text{sol}) \text{ for reactants}$$
 (8)

Multiconfigurational Self-Consistent Field (MCSCF). To make our computations tractable, DFT-optimized structures were used for further multiconfigurational calculations. All multiconfigurational calculations were performed as implemented in ORCA 4.2.<sup>47</sup> For better convergence, active orbitals for multiconfigurational calculations are derived from unrestricted natural orbitals. All CASSCF results were calculated using def2-TZVP basis on all atoms. The choice of the active space is the most critical decision in any CASSCF study. A general series of rules for how to choose appropriate active space for a transition-metal complex has been established elsewhere <sup>48,49</sup> and was generally followed here. All five d-orbitals and important ligand-based orbitals (e.g. PDI- $1\pi^*$  and PDI- $2\pi^*$ ) were included accordingly. Active space conservation of every single calculation was examined for proper convergence. To accelerate CASSCF calculations, we employed resolution of identity (RI) approximation with def2/J and def2-TZVP/C auxiliary basis sets. To simulate excited states, state-averaged CASSCF (SA-CASSCF) calculations with 10 roots for singlets and 10 roots for triplets were computed. With the optimized SA-CAS wavefunction, strongly contracted NEVPT2 (SC-NEVPT2) calculations were carried out accordingly in order to restore dynamic correlation energy missing in CASSCF results.

# **COMPOUND SYNTHESIS**

**Preparation of (**Ph2PPr**PDI)Fe (3):** Under a nitrogen atmosphere, a 20 mL scintillation vial was charged with 3.81 g of mercury (19.06 mmol) followed by 0.022 g of freshly cut sodium metal (0.953 mmol) in

approximately 5 mL of THF. This mixture was stirred for 20 min at room temperature until the cloudy gray suspension turned clear. To this Na-Hg mixture, a solution of **2** (0.158 g, 0.191 mmol) in THF ( $\sim$ 8 mL) was added. The color of the reaction mixture changed from purple to greenish brown within 15 h. After stirring for 48 h at room temperature, the reaction mixture was filtered through Celite to remove the byproduct NaBr. The solvent was removed under vacuum to obtain 0.105 g (0.156 mmol, 82%) of a greenish brown solid identified as **3**. Anal. for C<sub>39</sub>H<sub>41</sub>N<sub>3</sub>FeP<sub>2</sub>: Calcd. C, 69.94%; H, 6.18%; N, 6.28%. Found: C, 69.79%; H, 6.10%; N, 6.09%. <sup>1</sup>H NMR (400 MHz, benzene- $d_6$ ): 8.58 (d, J = 7.6 Hz, 2H, pryidine), 7.72 (t, J = 7.6 Hz, 1H, pyridine), 7.46 (t, J = 7.2 Hz, 4H, phenyl), 7.25 (t, J = 7.4 Hz, 4H, phenyl), 6.54 (m, 8H, phenyl), 5.70 (t, J = 7.1 Hz, 4H,  $CH_2$ ), 4.47 (d, J = 12.1 Hz, 2H,  $CH_2$ ), 3.42 (t, J = 11.9 Hz, 2H,  $CH_2$ ), 2.26 (m, 4H,  $CH_2$ ), 2.18 (t, J = 2.6 Hz, 6H,  $CH_3$ ). <sup>13</sup>C NMR (100.492 MHz, benzene- $d_6$ ): 144.89 (t, J = 4.5 Hz, aryl), 144.64 (t, J = 2.1 Hz, aryl), 144.39 (d, J = 9.4 Hz, aryl), 139.07 (d, J = 18.2 Hz, aryl), 138.88 (d, J = 17.8 Hz, aryl), 133.23 (t, J = 6.7 Hz, aryl), 131.81 (t, J = 4.8 Hz, aryl), 127.44 (t, J = 5.0 Hz, aryl), 113.46 (s, aryl), 113.27 (s, aryl), 56.12 (s,  $CH_2$ ), 28.95 (t, J = 9.4 Hz,  $CH_3$ ), 28.00 (s,  $CH_2$ ), 14.99 (s,  $CH_2$ ). <sup>31</sup>P NMR (202.47 MHz, benzene- $d_6$ ): 69.87 (s, Fe-P).

Preparation of (Ph2PPrPDI)Co (4): Under a nitrogen atmosphere, a 20 mL scintillation vial was charged with 0.435 g (0.7086 mmol) of Ph2PPrPDI and approximately 5 mL of THF. A separate solution consisting of 0.092 g (0.7086 mmol) of CoCl<sub>2</sub> in approximately 5 mL of THF was then added dropwise. Upon addition, the solution immediately turned from yellow to a deep forest green color and was allowed to stir for 2 h at 25 °C. Another 20 mL scintillation vial was charged with approximately 5 mL of THF, 14.17 g (70.86 mmol) of mercury, and 81.48 g (3.543 mmol) of freshly cut sodium. This mixture was stirred for 20 min at room temperature until the cloudy gray suspension turned clear. Two drops of cyclooctatetraene (COT) was then added. To this Na/Hg mixture, the deep forest green slurry obtained from the first addition was added dropwise and a color change was observed from green to deep red over the course of 20 min. After 16 h of stirring, the mixture was filtered through Celite to remove NaCl byproduct and the solvent was removed under vacuum. The resulting solid was re-dissolved in toluene and filtered to remove any residual NaCl. The solvent was removed under vacuum, the product was washed 5 times with 5 mL of Et<sub>2</sub>O, and dried in vacuo to obtain 0.173 g (0.267 mmol, 38%) of a deep red solid identified as 4. Recrystallization from a saturated solution of toluene at -35 °C afforded red crystals. Anal. for C<sub>39</sub>H<sub>41</sub>N<sub>3</sub>CoP<sub>2</sub>: Calcd. C, 69.64%; H, 6.14%; N, 6.25%. Found: C, 68.82%; H, 5.94%; N, 5.89%. Magnetic susceptibility (Evans NMR method, 25 °C):  $\mu_{eff} = 1.64 \mu_B$ . <sup>1</sup>H NMR (400 MHz, benzene-d<sub>6</sub>, 25 °C): 73.34 (363 Hz), 65.18 (446 Hz), 56.36 (610 Hz), 11.52 (103 Hz), 10.88 (897 Hz), 9.87 (913 Hz), -0.47 (142 Hz), -3.26 (166 Hz), -9.09 (221 Hz), -26.61 (183 Hz).

**Preparation of (**<sup>Ph2PP</sup>**PDI)Ni (5):** Under a nitrogen atmosphere, a 20 mL scintillation vial was charged with 0.0448 g (0.075 mmol) of <sup>Ph2PP</sup>PDI and approximately 5 mL of toluene. A separate solution consisting of 0.021 g (0.076 mmol) of Ni(COD)<sub>2</sub> in approximately 5 mL of toluene was then added

dropwise to the solution of Ph2PPrPDI. Upon adding Ni(COD)2, the solution immediately changed from the yellow color indicative of Ph2PPrPDI to a deep olive color. The resulting reaction mixture was then sealed and allowed to stir at 23 °C for 24 h. The resulting deep olive solution was filtered through Celite and the toluene was removed in vacuo to yield a green solid identified as 5. Recrystallization from an ether/pentane solution afforded 0.0307 g (61%) of transparent dark green crystals. Anal. for C<sub>39</sub>H<sub>41</sub>N<sub>3</sub>NiP<sub>2</sub>: Calcd. C, 69.66%; H, 6.15%; N, 6.25%. Found: C, 69.47%; H, 6.46%; N, 5.64%. Magnetic susceptibility (Evans NMR method, 25 °C):  $\mu_{eff} = 1.23 \,\mu_{B}$ . Magnetic susceptibility (balance, 25 °C):  $\mu_{\text{eff}} = 0.33 \ \mu_{\text{B}}$ . <sup>1</sup>H NMR (400 MHz, benzene- $d_6$ , 25 °C): 23.37 (875 Hz), 12.69 (402 Hz), -4.48

(6260 Hz).

# ASSOCIATED CONTENT

Supporting Information. The Supporting Information is available free of charge on the ACS Publications website. Crystallographic information, spectroscopic characterization, computational details, computed energies, vibrational frequencies and Cartesian coordinates of all DFT-optimized structures (PDF).

Accession Codes. CCDC 2083963-2083964 contain the supplementary crystallographic data for this paper. These data can be obtained free of charge via www.ccdc.cam.ac.uk/data request/cif, or by emailing data request@ccdc.cam.ac.uk or by contacting the Cambridge Crystallographic Data Centre, 12 Union Road, Cambridge CB2 1EZ, UK; fax: +44 1223 336033.

**AUTHOR INFORMATION** 

# **Corresponding Authors**

\*mbaik2805@kaist.ac.kr

\*ryan.trovitch@asu.edu

# **ORCID**

Jun-Hyeong Kim: 0000-0001-7747-5475

Sangho So: 0000-0002-2440-251X

Tyler M. Porter: 0000-0002-2693-2653

Anuja Sharma: 0000-0001-8563-8457

Marco Flores: 0000-0003-4139-7094

Mu-Hyun Baik: 0000-0002-8832-8187

Ryan J. Trovitch: 0000-0003-4935-6780

### **Author Contributions**

These authors equally contributed to this work.

# **Notes**

The authors declare no competing financial interests.

### **ACKNOWLEDGMENTS**

We thank the Institute for Basic Science (IBS-R10-A1) in Korea for financial support. This material is based upon work supported by the National Science Foundation under Grant No. 1651686. J.-H.K. thanks Mr. Gyumin Kang for fruitful discussions.

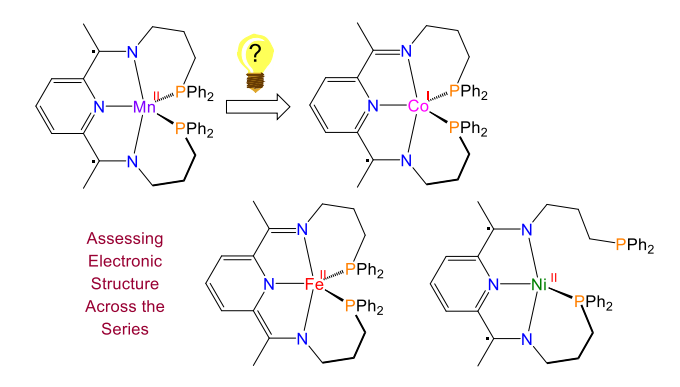
### REFERENCES

- 1. Ben-Daat, H.; Hall, G. B.; Groy, T. L.; Trovitch, R. J., Rational Design of Rhodium Complexes Featuring  $\kappa^4$ -N,N,N-and  $\kappa^5$ -N,N,P-Bis(imino)pyridine Ligands. *Eur. J. Inorg. Chem.* **2013**, 2013, 4430-4442.
- 2. Mukhopadhyay, T. K.; Flores, M.; Groy, T. L.; Trovitch, R. J., A Highly Active Manganese Precatalyst for the Hydrosilylation of Ketones and Esters. *J. Am. Chem. Soc.* **2014**, *136*, 882-885.
- 3. Knijnenburg, Q.; Gambarotta, S.; Budzelaar, P. H. M., Ligand-Centred Reactivity in Diiminepyridine Complexes. *Dalton Trans.* **2006**, 5442-5448.
- 4. Russell, S. K.; Bowman, A. C.; Lobkovsky, E.; Wieghardt, K.; Chirik, P. J., Synthesis and Electronic Structure of Reduced Bis(imino)pyridine Manganese Compounds. *Eur. J. Inorg. Chem.* **2012**, 2012, 535-545.
- 5. Mukhopadhyay, T. K.; Rock, C. L.; Hong, M.; Ashley, D. C.; Groy, T. L.; Baik, M.-H.; Trovitch, R. J., Mechanistic Investigation of Bis(imino)pyridine Manganese Catalyzed Carbonyl and Carboxylate Hydrosilylation. *J. Am. Chem. Soc.* **2017**, *139*, 4901-4915.
- 6. Trovitch, R. J., Comparing Well-Defined Manganese, Iron, Cobalt, and Nickel Ketone Hydrosilylation Catalysts. *Synlett* **2014**, *25*, 1638-1642.
- 7. Trovitch, R. J., The Emergence of Manganese-Based Carbonyl Hydrosilylation Catalysts. *Acc. Chem. Res.* **2017**, *50*, 2842-2852.
- 8. Mukhopadhyay, T. K.; Ghosh, C.; Flores, M.; Groy, T. L.; Trovitch, R. J., Hydrosilylation of Aldehydes and Formates Using a Dimeric Manganese Precatalyst. *Organometallics* **2017**, *36*, 3477-3483.
- 9. Yang, X.; Wang, C., Manganese-Catalyzed Hydrosilylation Reactions. *Chem. Asian J.* **2018**, *13*, 2307-2315.
- 10. Vasilenko, V.; Blasius, C. K.; Gade, L. H., One-Pot Sequential Kinetic Profiling of a Highly Reactive Manganese Catalyst for Ketone Hydroboration: Leveraging σ-Bond Metathesis via Alkoxide Exchange Steps. *J. Am. Chem. Soc.* **2018**, *140*, 9244-9254.
- 11. Carney, J. R.; Dillon, B. R.; Campbell, L.; Thomas, S. P., Manganese-Catalyzed Hydrofunctionalization of Alkenes. *Angew. Chem. Int. Ed.* **2018**, *57*, 10620-10624.
- 12. Alig, L.; Fritz, M.; Schneider, S., First-Row Transition Metal (De)Hydrogenation Catalysis Based On Functional Pincer Ligands. *Chem. Rev.* **2019**, *119*, 2681-2751.
- 13. Royo, B., Chapter Two Recent Advances in Catalytic Hydrosilylation of Carbonyl Groups Mediated by Well-Defined First-Row Late Transition Metals. In *Advances in Organometallic Chemistry*, Pérez, P. J., Ed. Academic Press: 2019; Vol. 72, pp 59-102.
- 14. Elsby, M. R.; Baker, R. T., Strategies and Mechanisms of Metal-Ligand Cooperativity in First-Row Transition Metal Complex Catalysts. *Chem. Soc. Rev.* **2020**, *49*, 8933-8987.
- 15. Bouwkamp, M. W.; Bowman, A. C.; Lobkovsky, E.; Chirik, P. J., Iron-Catalyzed  $[2\pi + 2\pi]$  Cycloaddition of  $\alpha,\omega$ -Dienes: The Importance of Redox-Active Supporting Ligands. *J. Am. Chem. Soc.* **2006**, *128*, 13340-13341.
- 16. Chirik, P. J.; Wieghardt, K., Radical Ligands Confer Nobility on Base-Metal Catalysts. *Science* **2010**, *327*, 794-795.
- 17. Lyaskovskyy, V.; de Bruin, B., Redox Non-Innocent Ligands: Versatile New Tools to Control Catalytic Reactions. *ACS Catal.* **2012**, *2*, 270-279.
- 18. Luca, O. R.; Crabtree, R. H., Redox-Active Ligands in Catalysis. *Chem. Soc. Rev.* **2013**, *42*, 1440-1459.

- 19. de Bruin, B.; Bill, E.; Bothe, E.; Weyhermüller, T.; Wieghardt, K., Molecular and Electronic Structures of Bis(pyridine-2,6-diimine)metal Complexes [ML<sub>2</sub>](PF<sub>6</sub>)<sup>n</sup> (n = 0, 1, 2, 3; M = Mn, Fe, Co, Ni, Cu, Zn). *Inorg. Chem.* **2000**, *39*, 2936-2947.
- 20. Bart, S. C.; Chłopek, K.; Bill, E.; Bouwkamp, M. W.; Lobkovsky, E.; Neese, F.; Wieghardt, K.; Chirik, P. J., Electronic Structure of Bis(imino)pyridine Iron Dichloride, Monochloride, and Neutral Ligand Complexes: A Combined Structural, Spectroscopic, and Computational Study. *J. Am. Chem. Soc.* **2006**, *128*, 13901-13912.
- 21. Römelt, C.; Weyhermüller, T.; Wieghardt, K., Structural Characteristics of Redox-Active Pyridine-1,6-diimine Complexes: Electronic Structures and Ligand Oxidation Levels. *Coord. Chem. Rev.* **2019**, *380*, 287-317.
- 22. The HOMO of 3 exhibits  $\pi$ -bonding between the metal and ligand; therefore, it is possible to argue that this compound features an Fe(0) center that is donating electron density to the PDI chelate through  $\pi$ -backbonding. The Fe-PDI  $\pi$ -antibonding orbitals (including the LUMO) are higher in energy and are not populated, a feature that would irrefutably indicate redox non-innocence. Regardless of the electronic structure description that is chosen, approximately two electrons worth of density is being transferred to PDI, and the physical or intrinsic oxidation state of iron is Fe(II). For an in depth discussion of intrinsic oxidation states, please see: Wolczanski, P. T., Flipping the Oxidation State Formalism: Charge Distribution in Organometallic Complexes As Reported by Carbon Monoxide. *Organometallics* **2017**, *36*, 622-631.
- 23. Fedorov, D. G.; Koseki, S.; Schmidt, M. W.; Gordon, M. S., Spin-Orbit Coupling in Molecules: Chemistry beyond the Adiabatic Approximation. *Int. Rev. Phys. Chem.* **2003**, *22*, 551-592.
- 24. Dede, Y.; Zhang, X.; Schlangen, M.; Schwarz, H.; Baik, M.-H., A Redox Non-innocent Ligand Controls the Life Time of a Reactive Quartet Excited State An MCSCF study of [Ni(H)(OH)]<sup>+</sup>. *J. Am. Chem. Soc.* **2009**, *131*, 12634-12642.
- 25. A negative value was obtained during measurement, indicative of diamagnetism. Small differences in calculating the diamagnetic corrections for  $^{Ph2PPr}PDI$  (not available in the literature) result in considerable differences in  $\mu_B$  due to the square root function in the following equation:  $\mu_{eff} = \sqrt{(8\chi_p T)}$ . For a related example see: Nasibipour, M.; Safaei, E.; Masoumpour, M. S.; Wojtczak, A., Ancillary Ligand Electro-Activity Effects towards Phenyl Acetylene Homocoupling Reaction by a Nickel(II) Complex of a Non-Innocent O-Amino Phenol Ligand: A Mechanistic Insight. *RSC Adv.* **2020**, *10*, 24176-24189.
- 26. Manuel, T. D.; Rohde, J.-U., Reaction of a Redox-Active Ligand Complex of Nickel with Dioxygen Probes Ligand-Radical Character. *J. Am. Chem. Soc.* **2009**, *131*, 15582-15583.
- 27. Zhu, D.; Thapa, I.; Korobkov, I.; Gambarotta, S.; Budzelaar, P. H. M., Redox-Active Ligands and Organic Radical Chemistry. *Inorg. Chem.* **2011**, *50*, 9879-9887.
- 28. Yang, L.; Powell, D. R.; Houser, R. P., Structural Variation in Copper(I) Complexes with Pyridylmethylamide Ligands: Structural Analysis with a New Four-coordinate Geometry Index,  $\tau_4$ . *Dalton Trans.* **2007**, 955-964.
- 29. Mukhopadhyay, T. K.; MacLean, N. L.; Flores, M.; Groy, T. L.; Trovitch, R. J., Isolation of Mn(I) Compounds Featuring a Reduced Bis(imino)pyridine Chelate and Their Relevance to Electrocatalytic Hydrogen Production. *Inorg. Chem.* **2018**, *57*, 6065-6075.
- 30. Weil, J. A.; Bolton, J. R., *Electron Paramagnetic Resonance: Elementary Theory and Practical Applications*. John Wiley & Sons: 2007; p 688.
- 31. Stoll, S.; Schweiger, A., EasySpin, A Comprehensive Software Package for Spectral Simulation and Analysis in EPR. *J. Magn. Reson.* **2006**, *178*, 42-55.
- 32. Parr, R. G.; Yang, W., Density-Functional Theory of Atoms and Molecules. *Oxford University Press, New York* **1994**, *3*, 14312-14321.
- 33. Bochevarov, A. D.; Harder, E.; Hughes, T. F.; Greenwood, J. R.; Braden, D. A.; Philipp, D. M.; Rinaldo, D.; Halls, M. D.; Zhang, J.; Friesner, R. A., Jaguar: A High-Performance Quantum Chemistry Software Program with Strengths in Life and Materials Sciences. *Int. J. Quantum Chem.* **2013**, *113*, 2110-2142.
- 34. Zhao, Y.; Truhlar, D. G., The M06 Suite of Density Functionals for Main Group Thermochemistry, Thermochemical Kinetics, Noncovalent Interactions, Excited States, and Transition Elements: Two New Functionals and Systematic Testing of Four M06-Class Functionals and 12 Other Functionals. *Theor. Chem. Acc.* **2008**, *120*, 215-241.

- 35. Ditchfield, R.; Hehre, W. J.; Pople, J. A., Self-Consistent Molecular-Orbital Methods. IX. An Extended Gaussian-Type Basis for Molecular-Orbital Studies of Organic Molecules. *J. Chem. Phys.* **1971,** *54*, 724-728.
- 36. Hay, P. J.; Wadt, W. R., Ab Initio Effective Core Potentials for Molecular Calculations. Potentials for the Transition Metal Atoms Sc to Hg. *J. Chem. Phys.* **1985**, *82*, 270-283.
- 37. Wadt, W. R.; Hay, P. J., Ab Initio Effective Core Potentials for Molecular Calculations. Potentials for Main Group Elements Na to Bi. *J. Chem. Phys.* **1985**, *82*, 284-298.
- 38. Hay, P. J.; Wadt, W. R., Ab Initio Effective Core Potentials for Molecular Calculations. Potentials for K to Au Including the Outermost Core Orbitals. *J. Chem. Phys.* **1985**, *82*, 299-310.
- 39. Slater, J. C., *The Self-Consistent Field for Molecules and Solids: Quantum Theory of Molecules and Solids.* McGraw-Hill Book Company: 1974.
- 40. Vosko, S. H.; Wilk, L.; Nusair, M., Accurate Spin-Dependent Electron Liquid Correlation Energies for Local Spin Density Calculations: A Critical Analysis. *Can. J. Phys.* **1980**, *58*, 1200-1211.
- 41. Becke, A. D., Density-Functional Exchange-Energy Approximation with Correct Asymptotic Behavior. *Phys. Rev. A* **1988**, *38*, 3098-3100.
- 42. Lee, C.; Yang, W.; Parr, R. G., Development of the Colle-Salvetti Correlation-Energy Formula into a Functional of the Electron Density. *Phys. Rev. B* **1988**, *37*, 785-789.
- 43. Becke, A. D., Density-Functional Thermochemistry. III. The Role of Exact Exchange. *J. Chem. Phys.* **1993**, *98*, 5648-5652.
- 44. Grimme, S.; Antony, J.; Ehrlich, S.; Krieg, H., A Consistent and Accurate Ab Initio Parametrization of Density Functional Dispersion Correction (DFT-D) for the 94 Elements H-Pu. *J. Chem. Phys.* **2010**, *132*, 154104.
- 45. Slater, J. C.; Phillips, J. C., Quantum Theory of Molecules and Solids Vol. 4: The Self-Consistent Field for Molecules and Solids. *Phys. Today* **1974**, *27*, 49.
- 46. Dunning, T. H., Gaussian Basis Sets for Use in Correlated Molecular Calculations. I. The Atoms Boron through Neon and Hydrogen. *J. Chem. Phys.* **1989**, *90*, 1007-1023.
- 47. Neese, F.; Wennmohs, F.; Becker, U.; Riplinger, C., The ORCA Quantum Chemistry Program Package. *J. Chem. Phys.* **2020**, *152*, 224108.
- 48. Veryazov, V.; Malmqvist, P. Å.; Roos, B. O., How to Select Active Space for Multiconfigurational Quantum Chemistry? *Int. J. Quantum Chem.* **2011**, *111*, 3329-3338.
- 49. Pierloot, K., The CASPT2 Method in Inorganic Electronic Spectroscopy: From Ionic Transition Metal to Covalent Actinide Complexes. *Mol. Phys.* **2003**, *101*, 2083-2094.

# **Table of Contents Graphic**



Commercialization of the bis(imino)pyridine manganese compound, (Ph2PPrPDI)Mn, inspired the synthesis of low-valent iron, cobalt, and nickel compounds that feature the same ligand framework. Ligand redox non-innocence has been observed across the series; however, differences in chelate denticity and electronic structure are also described.